

MAPPING THE STELLAR STRUCTURE OF THE MILKY WAY

JELTE T. A. DE JONG¹, BRIAN YANNY², HANS-WALTER RIX¹, ANDREW E. DOLPHIN³, NICOLAS F. MARTIN¹, TIMOTHY C. BEERS⁴*Draft version October 27, 2019*

ABSTRACT

We map the stellar structure of the Galaxy by applying color-magnitude diagram fitting to photometric data from the SEGUE survey. The SEGUE imaging scans allow, for the first time, a comprehensive analysis of Milky Way structure at both high and low latitudes using uniform SDSS photometry. The advantage of color-magnitude diagram fitting is that it incorporates photometry of all relevant stars simultaneously, bypassing the need to choose single tracer populations. Using three template stellar populations we obtain a sparse 3-dimensional map of the stellar mass distribution. Fitting a smooth Milky Way model, comprised of exponential thin and thick disks and an axisymmetric power-law halo, allows us to constrain the structural parameters of the thick disk and halo. The thick disk scale height and length of such models are well constrained at 0.75 ± 0.07 kpc and 4.1 ± 0.4 kpc, respectively. We find a stellar halo flattening within ~ 25 kpc of $c/a = 0.88 \pm 0.03$ and a power-law index of 2.75 ± 0.07 (for $7 \text{ kpc} \lesssim R_{GC} \lesssim 30 \text{ kpc}$). The mass density of the thick disk and halo components are best constrained at 2.5 kpc and 12.5 kpc above the plane, respectively. The model fits, averaging over any substructures, yield densities at the solar location of $\rho_{thick,\odot} = 10^{-2.3 \pm 0.1} M_{\odot} \text{pc}^{-3}$ and $\rho_{halo,\odot} = 10^{-4.20 \pm 0.05} M_{\odot} \text{pc}^{-3}$, in good agreement with previous determinations. We detect in-situ evidence for a metallicity gradient in the stellar halo: within $R \lesssim 15$ kpc the stellar halo has a mean metallicity of $[Fe/H] \simeq -1.6$, which shifts to $[Fe/H] \simeq -2.2$ at larger radii, in line with the two-component halo predictions of Carollo et al. (2007). Subtraction of the best-fit smooth and symmetric model from the density maps reveals a wealth of substructures at all latitudes, some attributable to known streams and overdensities, and some new. A simple warp cannot account for the low latitude substructure, as overdensities occur simultaneously above and below the Galactic plane.

Subject headings: Galaxy: structure – Galaxy: disk – Galaxy: halo – stars: statistics

1. INTRODUCTION

Studying the stellar structure of the Milky Way has a long history, as early models based on star counts were already constructed by the likes of Herschel (1785) and Kapteyn (1922). Today we know that four ‘components’ make for a sensible approximate description of the Milky Way stellar body, each with different structural, kinematic and population characteristics: the bulge, the thin and the thick disk, and the stellar halo. Determining the properties of these components accurately is a difficult undertaking, as it requires surveys with sufficient sky coverage to assess the overall geometry, sufficient depth for mapping stars to ~ 10 to 30 kpc and sufficient information (e.g. color-based luminosity estimates) to get reasonable distances for these stars. Furthermore, the presence of dust in the plane of the disk clouds our view of most of the Galaxy at wavelengths shorter than a few microns. For this reason, most previous efforts to study Milky Way structure at low latitudes have used (near-)infrared data, such as the work by Kent et al. (1991)

based on data from the Spacelab infrared telescope, or more recent work using 2MASS data (e.g. Momany et al. 2006; Reyl   et al. 2009). Dust extinction is much less severe at near-infrared wavelengths, but these surveys are less sensitive than current optical surveys and often rely on tracer populations with less accurate distances.

Beyond the global parameters, the detailed substructure of the Milky Way components tell us something about how the Milky Way formed and evolved: as galaxies form through subsequent mergers and accretions of smaller systems, these events leave identifiable signatures in their structure and kinematics. This also has cosmological implications, as the structure of the dark halo and the interactions with dark subhalos can significantly influence the appearance of a galaxy (e.g. Kazantzidis et al. 2007; Younger et al. 2008).

Over the past years, data from 2MASS and SDSS have played a key role in revolutionizing our empirical picture of these stellar components by demonstrating the level of substructure they exhibit (Newberg et al. 2002; Belokurov et al. 2006; Grillmair 2006; Belokurov et al. 2007; Juri   et al. 2008; Bell et al. 2008). Much of the work using SDSS data has focused away from the bulk of the Milky Way’s stars to high galactic latitudes. Nonetheless, Juri   et al. (2008) have been able to constrain the structural parameters of the stellar halo and the thin and thick disk. At lower galactic latitudes, the discovery of substructure in the stellar disk (Newberg et al. 2002; Ibata et al. 2003; Martin et al. 2004; Conn et al. 2005, 2007; Bellazzini et al. 2006) has

Electronic address: dejong@mpia.de

¹ Max-Planck-Institut f  r Astronomie, K  nigstuhl 17, D-69117 Heidelberg, Germany² Fermi National Accelerator Laboratory, P.O. Box 500, Batavia, IL 60510, United States³ Raytheon Company, 1151 E Hermans Rd, Tucson, AZ 85756, United States⁴ Department of Physics & Astronomy and JINA: Joint Institute for Nuclear Astrophysics, Michigan State University, E. Lansing, MI, 48824, USA

led to a vigorous debate as to both the geometry and the origin of the seemingly complex deviations from simple, symmetric disk models.

In this paper we derive a new map of the stellar distribution in the Milky Way. Though covering only the Northern celestial hemisphere, and that only sparsely, this map covers both high and low latitudes and uses rigorously derived stellar distances. This map is based on one of the constituent projects of the extended SDSS survey (SDSS II), SEGUE (Sloan Extension for Galactic Understanding and Exploration, Yanny et al. 2009a), which is an imaging and spectroscopic survey aimed at the study of the MW and its stellar populations. Whereas the main SDSS survey avoided low Galactic latitudes, SEGUE imaging scans go through the Galactic plane (see Figure 1), allowing a ‘picket-fence’ view of the Galaxy at these low latitudes. It is this deep, uniform data set that enables a systematic analysis of stellar structure and substructure as function of Galactic latitude and longitude, which we base on color-magnitude diagram (CMD) fitting techniques developed in de Jong et al. (2008). A crucial advantage of an analysis based on CMDs is that they bypass the often ad-hoc and sometimes problematic choices of stellar ‘tracers’ (such as K-dwarfs or F-stars) to delineate the structure. Instead, this procedure results immediately in a mass density map for stellar population components of, say, different metallicity.

To avoid having to fit the complex stellar population make-up of the thin disk, we in the end consider only stars that are more than 1 kpc away from the Galactic mid-plane, and treat the thin disk as a small perturbation to our results. As SEGUE is a northern hemisphere survey, it stays far away from the Galactic bulge, which can be safely ignored. On the one hand, the resulting maps of stellar mass density in the halo and disk allow us to put constraints on the structural parameters of these Galactic components. On the other hand, subtracting a smooth galactic model reveals a wealth of substructure, especially at low latitudes, which we will study in detail in a forthcoming publication.

The outline of this paper is as follows. §2 describes the data used for our analysis, and §3 describes the CMD-fitting techniques we utilize. The resulting stellar distributions are presented in §4, where we also fit smooth Galactic models to them and look at deviations from the best fitting model. Finally, we summarize and discuss our results in §5.

2. SEGUE PHOTOMETRY AND COVERAGE

As part of the SEGUE survey (Yanny et al. 2009a), ten 2.5° -wide scans, crossing the Galactic plane at fixed longitudes, were imaged in five passbands (u , g , r , i , and z ; Gunn et al. 1998, 2006; Hogg et al. 2001). These data are available as part of SDSS Data Release 7 (DR7, Abazajian et al. 2009). An automated data reduction and analysis pipeline produces accurate astrometric and photometric measurements for all detected objects (Lupton, Gunn, & Szalay 1999; Stoughton et al. 2002; Smith et al. 2002; Pier et al. 2003; Ivezić et al. 2004; Tucker et al. 2006), reaching a photometric accuracy of 2% down to $g \simeq 22.5$ and $r \simeq 22$ (Ivezić et al. 2004; Sesar et al. 2007). In Figure 1 the coverage of the scans between Galactic latitudes of $+50^\circ$ and -50° is

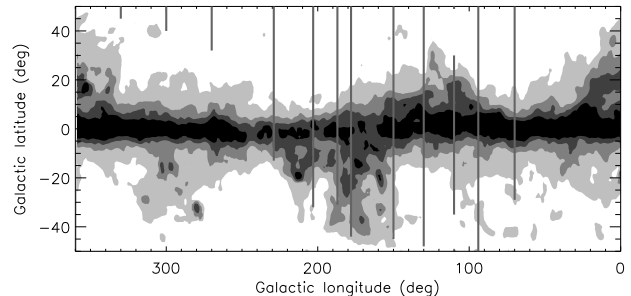


FIG. 1.— Overview of low-latitude imaging scans from SEGUE (Yanny et al. 2009a) used for this analysis, shown as the vertical lines in Galactic coordinates. The grayscale shows dust reddening estimates based on the extinction maps from Schlegel et al. (1998), with increasingly dark regions corresponding to $E(B - V) > 0.1$, 0.25, 0.5 and 1.0 mag. Only regions with $E(B - V) \leq 0.25$ are used in the analysis.

shown. Most scans have some overlap with the SDSS main survey or SDSS Legacy area in the North Galactic cap, and we extract 2.5° -wide strips of data from DR7 to extend the photometry to Galactic latitudes of 85° . For the CMD fitting analysis we restrict ourselves to the two bands, g and r , that are most sensitive to population/distance analyses. The SEGUE imaging in DR7 have been photometrically calibrated following the procedure of Padmanabhan et al. (2008). The procedure basically uses the overlap of the SEGUE data scans with the Legacy SDSS imaging scans to solve for the photometric zero-points and flat-field co-efficients of the SDSS 2.5m camera system. This overlap generally occurs in uncrowded regions of sky ($|b| > 20^\circ$) even for scans which extend to cross the Galactic plane. The photometric solution for the SEGUE scans was done incrementally rather than globally after the global solution for all the SDSS Legacy scans. The accuracy of the photometry is estimated to be to about 1.5% in g , and r ($< 2\%$ in color). See §2.2 of Yanny et al. (2009a) for more details on the SEGUE imaging and calibration. We de-redden all data using the dust maps from Schlegel et al. (1998), including the correction suggested by Bonifacio et al. (2000), provided through the SDSS catalog server. As most of the dust is confined close to the Galactic plane it is in the foreground for all stars more distant than 1 kpc from the mid-plane, which we will use in our analysis.

To illustrate the basis for our subsequent modelling, several de-reddened CMDs drawn from different latitudes in the SEGUE stripe at $l=94^\circ$ are shown in Figure 2. The most obvious difference between different latitudes is the variation in reddening, which ranges from an $E(B - V)$ of up to several magnitudes very close to or in the plane of the Galaxy to a few hundredths of a magnitude at high latitudes. Once the reddening reaches several tenths of magnitudes (e.g. upper right panel of Fig. 2), the unaccounted differential reddening along the line of sight smears out the CMD features. For this reason, and because the dereddening itself is less reliable in high extinction regions, we exclude regions with $E(B - V) > 0.25$ from our analysis; the excluded regions correspond to the three darkest shadings in Fig. 1. Hence, the two lower panels in Figure 2 are representative for the CMDs used for this study. This cut in foreground extinction also means that we exclude the most crowded regions

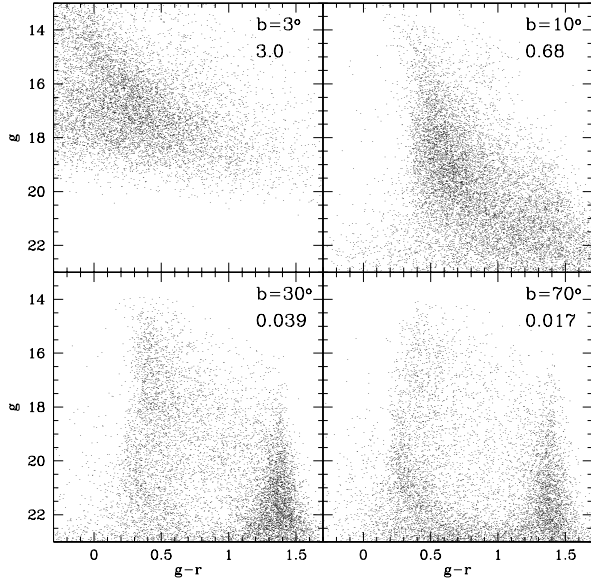


FIG. 2.— Typical color-magnitude diagrams taken from the SEGUE imaging scan at $l=94^\circ$, dereddened based on the dust extinction maps from Schlegel et al. (1998). In the upper right corner of each panel the Galactic latitude and the average reddening in $E(B-V)$ (Schlegel et al. 1998) corresponding to each CMD are indicated. The latitude range from which the CMDs were extracted were chosen so that each contains approximately the same number of stars.

and thus avoid possible problems due to crowding.

Before a more formal CMD analysis, it is instructive to describe the main features seen in the CMDs and to realize which kind of stars they contain. Figure 3 shows the number density of stars in bins in the color-magnitude plane, or Hess diagram, of all stars in the SEGUE scan at $l=94^\circ$ and $b > 30^\circ$. The large concentration of stars in the lower right, i.e. at faint magnitudes and centered at a $g-r$ color of ~ 1.4 consists of nearby, intrinsically faint and low-mass dwarf stars in the disk. The other plume of stars at $g-r \sim 0.4$ is where the main-sequence turn-off (MSTO) stars of old ($\gtrsim 10$ Gyr) stellar populations lie. A shift in the average color of this plume of stars is visible around $g=18$. This is caused by the difference in metallicity between the thick disk, which dominates at brighter magnitudes, and the Galactic halo, dominating at larger distances. The color of the MSTO is a useful proxy for the metallicity of the dominant population at a certain distance (e.g. see the discussion about this for SDSS isochrones in Girardi et al. 2004). Assuming a regular and smooth Milky Way, the main change between different latitudes are the relative contributions of halo and (thick) disk stars to the CMD. For example, comparing the CMDs corresponding to latitudes of 30° and 70° (lower panels of Fig. 2) shows how the number of disk stars decreases with respect to the halo stars. The field at 70° latitude adds complexity to this description, as it contains an example of stellar substructure, as the main-sequence feature produced by the Sagittarius stream is readily visible, running from $(g-r, g) \simeq (0.2, 20.0)$ to $(0.5, 22.0)$.

For our analysis of stellar structure, we divide the 2.5° -wide SEGUE stripes into bins of 1 degree width in latitude from which CMDs are created. Each CMD is then analysed as described in the next Section.

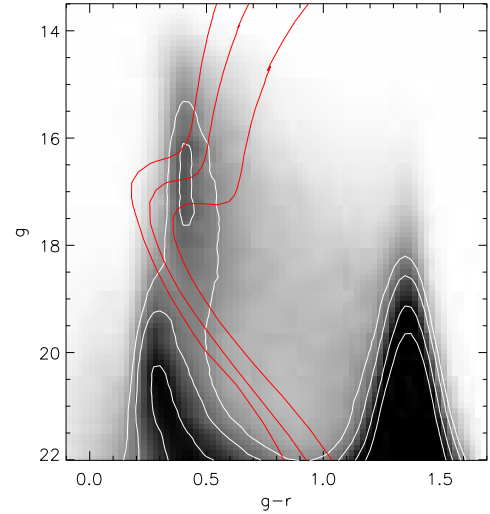


FIG. 3.— A Hess diagram (greyscale) of the SEGUE scan at $l=94^\circ$ and $b > 30^\circ$, in dereddened ($g, g-r$). Overplotted are isochrones corresponding to the three template stellar populations fit to the data. From right to left the isochrones are for the ‘thick-disk-like’ ($[\text{Fe}/\text{H}]=-0.7$), the ‘inner-halo-like’ intermediate metallicity ($[\text{Fe}/\text{H}]=-1.3$) and the ‘outer-halo-like’ metal-poor ($[\text{Fe}/\text{H}]=-2.2$) populations.

3. DISTANCE FITTING OF CMDS

In most applications of CMD fitting, observed photometry is compared with models in order to determine which combination of simple stellar populations best resembles the data, thereby providing a model of the star formation history (SFH) and age-metallicity relation (AMR). For the work presented here, we fit model stellar population CMDs based on the isochrones in SDSS filters provided by Girardi et al. (2004) to the SEGUE photometry. The software package we use for this (MATCH, Dolphin 1997, 2001) uses a maximum-likelihood method to determine the best linear combination of models, after transforming both models and data to Hess diagrams (2D histograms of stars in the color-magnitude plane), enabling a pixel-by-pixel comparison. For a proper comparison, the models need to be convolved with a realistic photometric error and completeness model. The model we use here is the same as in de Jong et al. (2008), based on the photometric errors from the SDSS pipeline (Ivezić et al. 2004) and the completeness determined from a comparison⁵ between SDSS and COMBO-17⁶. Since foreground reddening precludes the use of the most crowded regions in the mid-plane, crowding does not significantly affect the completeness in the data used here.

Rather than determining the SFH and AMR, our aim in the present context is to map the structure of the stellar populations in the outer MW. For this, we use the distance-fitting option of MATCH, described and tested in de Jong et al. (2008). To limit the number of free parameters and parameter degeneration in the fits, we want to define a small set of template stellar populations. The choice of templates is motivated both by the populations we expect to be present in the outer disk and inner halo, and by the CMD features we have to fit. As discussed

⁵ See <http://www.sdss.org/dr5/products/general/completeness.html>

⁶ http://www.mpia.de/COMBO/combo_index.html

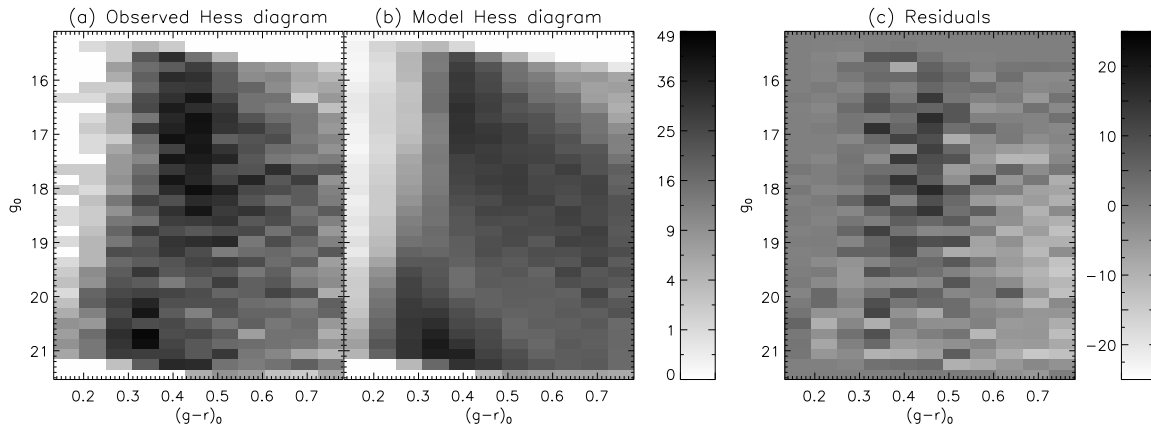


FIG. 4.— Example of distance distribution fitting, based on the Hess/CMD diagram at $l=94^\circ$ and $b=+30^\circ$; note that only the blue portion of the full color range in Figure 3 is shown here. No attempt to model low-mass thin disk stars dominating at $g-r > 0.8$ is made here. (a) Observed distribution of stars in the color-magnitude plane. (b) Best-fit model to (a), consisting of a combination of template stellar populations at different distances. (c) Residuals after subtracting the model (b) from the data (a). Color bars indicate the number of stars in the Hess diagram bins. The mean residuals across the CMD are $\sim 25\%$ of the mean star counts across the entire CMD.

in §2 the most obvious indicator of population differences will be the MSTO color, which means the templates should span the expected color range, preferably in regular intervals. The MSTO color of a stellar population depends both on its age and metallicity, but since both the thick disk and the halo stellar populations are known to be old, we choose to use a fixed age range and use metallicity offsets to probe the MSTO color range. We adopt three different metallicity bins, $[\text{Fe}/\text{H}] = -0.7, -1.3$ and -2.2 , respectively. All template populations have the same age range of $10.1 < \log[t/\text{yrs}] < 10.2$, and an assumed binary fraction of 0.5. For convenience, we choose a nomenclature for these components that is based on previous work: we refer to $[\text{Fe}/\text{H}] = -0.7$ as a thick-disk-like population and, following Carollo et al. (2007) to the $[\text{Fe}/\text{H}] = -1.3$ and -2.2 populations as the two halo populations, namely an inner-halo-like and outer-halo-like population, respectively. Note, however, that in our subsequent analysis this choice of terms neither immediately prejudices the geometry, nor implies that these components are ‘distinct’. We simply presume that these three components are sufficient to completely describe the stellar populations at any point that is at least 1 kpc above or below the Galactic mid-plane. Isochrones corresponding to these population templates are overplotted on Figure 3. The colors of the MSTO of populations 1 and 2 match the color of the prominent upper and lower plume of MSTO stars in Figure 3, respectively, while the third population has a bluer MSTO. Using a coarse grid of metallicities means that for stars with a metallicity different from any of the template populations a discrepant distance is inferred, as the brightness of the MS depends is metallicity dependant (see Fig. 3). The magnitude offsets in this case are ~ 0.3 and ~ 0.5 magnitudes, going from the highest ($[\text{Fe}/\text{H}] = -0.7$) to the lowest metallicity ($[\text{Fe}/\text{H}] = -2.2$) isochrone. As stars with intermediate metallicities will be interpolated between the template populations, this translates into distance uncertainties of at most 10%.

We deliberately choose to avoid fitting the thin disk, because a template population with more typical thin disk populations should have a large range in age and

metallicity and would be difficult to distinguish from a combination of the three templates described above. Hence, when presenting and interpreting our results, we will ignore the distance ranges where the thin disk is expected to be an important contribution to the star counts, and only consider regions with $Z > 1.0$ kpc, or roughly four thin disk scale heights.

All stars with $15 < g < 21.5$, $15 < r < 21.0$ and $0.1 < g-r < 0.8$ are used in the fits, with Hess diagram pixel sizes of 0.07 in color and 0.2 in magnitude. The color-cut of $g-r < 0.8$ eliminates the issue of fitting the faint, red thin-disk stars. For each of the templates, model CMDs are created for a range of distance moduli. The magnitude limits used in the fits ($15 < g < 21.5$) correspond to distance limit for MSTO stars of roughly $1.5 < D < 25$ kpc. Since the MSTO stars provide the best constraints for these CMD fits, only this distance range will be analysed. However, to avoid edge effects, model templates are created for distance moduli between 5.0 (100 pc) to 20.0 (100 kpc) in steps of 0.2 mag ($\sim 10\%$ distance bins). MATCH then determines the best-fitting combination of model CMDs. Subsequently, the uncertainties on the obtained results are determined by refitting Monte Carlo realizations of each CMD drawn from its best-fit model, as described in Dolphin (2001). It is again important to note the difference between this approach and using stars of a particular spectral type to make 3D maps of the Milky Way (as in e.g. Jurić et al. 2008). The CMD fitting will give a direct, high signal-to-noise map of the stellar mass density, even if the stellar populations are spatially varying. This approach also utilizes the information for stars of different spectral types (colors, luminosities) simultaneously.

A comparison of the best-fit model with the CMD data for the region at $l=94^\circ$ and $b=+30^\circ$ (the same field as shown the lower left panel in Figure 2) is presented in Figure 4. Although the model is not perfect (which perhaps should not be expected due to the simple model population make-up), the general features of the density distribution are well-reproduced. The mean residuals are 25% of the mean star counts across the portion of the CMD used in the fit.

4. RESULTS

Rather than the stellar mass or the number of stars, the CMD fitting software provides the star formation rate (SFR) in $M_\odot \text{yr}^{-1}$ corresponding to each population template for each distance modulus bin. However, these SFRs can easily be converted to the spatial stellar mass density using,

$$\rho_{*,i} = \frac{3}{\omega(D_2^3 - D_1^3)} \times SFR_i \Delta t, \quad (1)$$

where SFR_i is the star formation rate (SFR) in $M_\odot \text{yr}^{-1}$ of the i th template population, Δt is the width of the age bin, ω the solid angle in steradian corresponding to each CMD, and D_2 and D_3 the distances corresponding to the limits of the distance modulus bin. The 2001 MATCH version uses a single power-law initial mass function (IMF). In this analysis we opt for a Salpeter IMF (Salpeter 1955) with cutoffs at 0.1 and 120 M_\odot , which yields a total mass of about a factor 2 higher than currently favored IMFs (e.g. Kroupa et al. 1993) for old populations (see also Martin et al. 2008). It should also be kept in mind that these masses correspond to the total mass of stars formed, which especially for old populations does not correspond to the total mass in stars today, but rather to the total mass in both stars and stellar remnants.

Figure 5 shows the stellar mass densities obtained from the CMD fits for each of the stripes, summed over all three metallicities. Figure 6 shows the same, but with a color-coding that represents the relative contributions of the three different template populations. Generally speaking, the stellar density decreases in a continuous fashion with increasing distance from the Galactic center and plane, although some deviations are noticeable. For example, a region of apparent excess density extends to the bottom of the $l=94^\circ$ panel in Figure 5, which is caused by the Sagittarius stream (Majewski et al. 2003; Yanny et al. 2009b). The contributions of the three different template populations change as expected. With increasing distance from the Sun, the ‘thick disk’, ‘inner halo’ and ‘outer halo’ populations dominate in turn. The galactocentric distance where the metal-poor ‘outer halo’ starts dominating over the more metal-rich inner halo varies between 10 and 20 kpc.

In Figure 7 we show the mean density and mass-weighted metallicity as a function of distance from the Sun for a set of different bins in Galactic latitude in the form of graphs. Apart from the total mass density, the contributions from the individual template populations are also plotted. The increasing contribution of the thick disk to the density along lines of sight with decreasing latitude is clearly visible, both in the density graphs and in the steepness of the metallicity gradient at distances less than 10 kpc. The metallicity graphs indicate that the stellar halo has an average metallicity of $[\text{Fe}/\text{H}] \simeq -1.6$ at distances less than ~ 15 kpc, confirming the findings of Ivezić et al. (2008), but then drops to $[\text{Fe}/\text{H}] \lesssim -2$ further out. Although the transition is smooth, and both ‘halo-like’ template populations contribute to the mass density at every distance, such a drop is consistent with the presence of two distinct populations, as predicted by Carollo et al. (2007). Recall, however, that the transitions between different templates can only be taken as direct evidence of a metallicity gradient in the halo, if

age differences between halo stars play no role in their turn-off color.

The stellar density maps are also presented in Table 1. As the table contains 25 476 rows, only the first five rows are printed, with the complete table available in electronic form online.

4.1. Smooth Galactic model fits

To describe the stellar density maps quantitatively, we fit a model to the maps in Figure 5. Any substructures that are present on top of a ‘smooth’ stellar distribution should become apparent after subtraction of the best-fit model. The model we use consists of a double exponential thin disk and thick disk (Bahcall & Soneira 1980; Gilmore & Reid 1983), and an axisymmetric power-law halo (Eggen et al. 1962; Chiba & Beers 2000; Jurić et al. 2008):

$$\begin{aligned} \rho(R, Z) = & \rho_{thin,\odot} \left(e^{R_\odot/L_1} \exp\left(-\frac{R}{L_1} - \frac{Z}{H_1}\right) \right. \\ & + f_{thick,\odot} e^{R_\odot/L_2} \exp\left(-\frac{R}{L_2} - \frac{Z}{H_2}\right) \\ & \left. + f_{halo,\odot} \left(\frac{R_\odot}{\sqrt{R^2 + (Z/q_h)^2}} \right)^{n_h} \right). \end{aligned} \quad (2)$$

Here, R_\odot is the distance from the Sun to the Galactic center; L_{thin} , H_{thin} , L_{thick} and H_{thick} are the scale lengths and heights of the thin and thick disk; q_{halo} and n_{halo} are the halo flattening and power-law exponent; finally, $\rho_{thin,\odot}$ is the local thin disk density and $f_{thick,\odot}$ and $f_{halo,\odot}$ the local density fraction of the thick disk and halo relative to the thin disk. In light of the results of Bell et al. (2008) there seems to be no need for a more sophisticated, for example triaxial, halo model. For a grid of parameter values, models are compared to the density maps. Since the density maps contain bins in distance and Galactic latitude, and each bin has an uncertainty from the Monte Carlo test, the χ^2 goodness-of-fit can be determined straightforwardly as

$$\chi^2 = \sum_i \left(\frac{\rho_{i,model} - \rho_{i,observed}}{\sigma_{i,observed}} \right)^2. \quad (3)$$

As mentioned before, we only use the bins for which $1.5 < D < 25$ kpc and $Z > 1.0$ kpc.

Some localized stellar overdensities are known to exist in the Milky Way which may be strong enough to affect significantly the attempt to fit a ‘smooth’ model. The strongest one in the halo is the Sagittarius stream, presumed tidal debris from the Sagittarius dwarf galaxy. It arcs through the North Galactic cap through the stripes at $l=229^\circ$, 270° , 300° , and 330° at high latitudes (Belokurov et al. 2006), and intersects the stripes at $l=94^\circ$ and 178° at negative latitudes (Majewski et al. 2003; Yanny et al. 2009b). This can already be seen in the density maps in Figure 5, for example at $l=94^\circ$, $Z < -15$ kpc and $D < 10$ kpc. At lower latitudes the largest known overdensity is the Monoceros overdensity, discovered by Newberg et al. (2002) and of still controversial origin. It may plausibly be part of the Low Latitude or anti-center stream, a ring-like structure thought to encircle the Milky Way completely (Ibata et al. 2003).

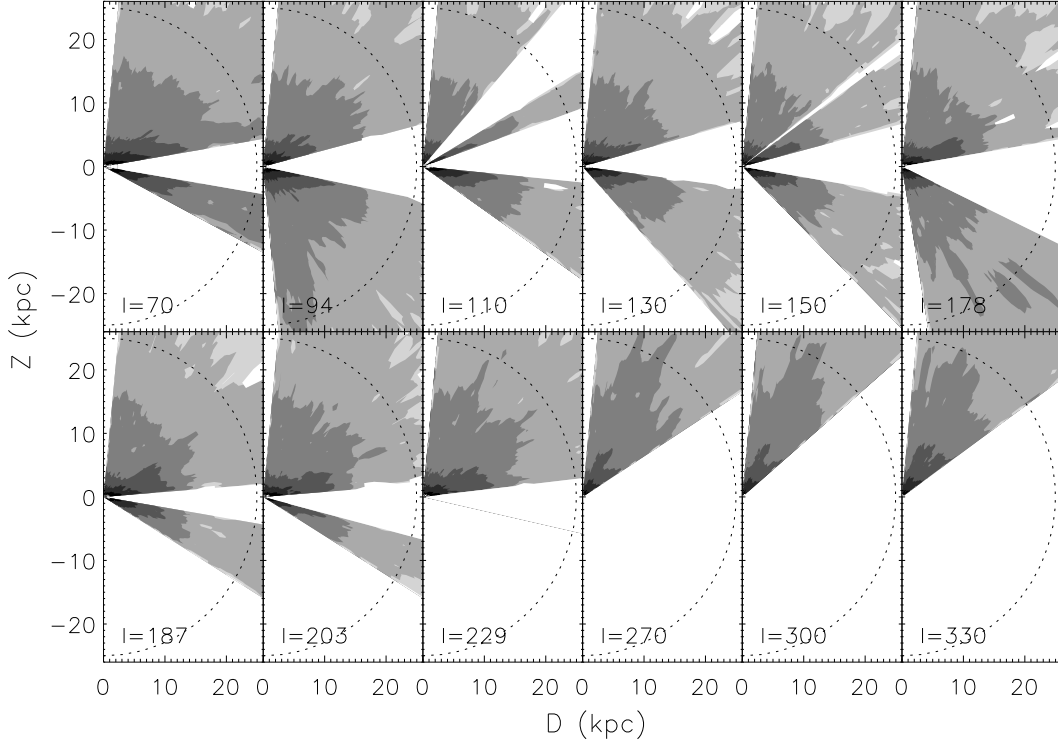


FIG. 5.— Tomography of the Milky Way. Shown are maps of the stellar mass density in a set of slices of constant l , drawing on the single population fits, as function of distance from the Sun, and height above or below the Galactic plane, in kpc. Contours correspond to steps of a factor 10 in stellar mass density. Each panel shows a different imaging scan, the Galactic longitude of which is listed at the bottom, and darker gray levels correspond to higher densities. The dashed semicircles show the maximal distance to which fit results are (mainly) based on main-sequence turn-off star colors and densities.

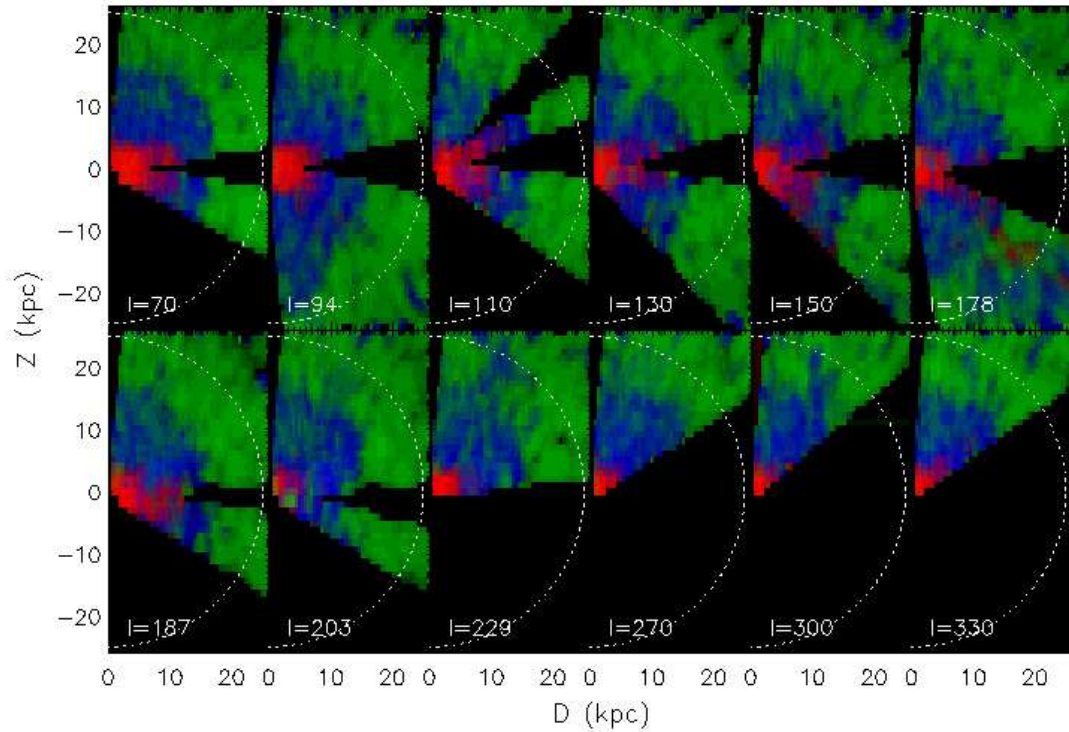


FIG. 6.— Density-metallicity tomography: shown is the distribution of stellar populations from the triple population fits with the same layout as in Fig. 5. The thick-disk-like population with $[\text{Fe}/\text{H}] \simeq -0.7$ is color-coded as red, the inner halo-like population with $[\text{Fe}/\text{H}] \simeq -1.3$ as blue, and the outer halo-like population with $[\text{Fe}/\text{H}] \simeq -2.2$ as green. The white, dashed semicircles show the distance up to where fit results are (mainly) based on main-sequence turn-off star colors and densities.

TABLE 1
STELLAR DENSITY MAPS

l ($^{\circ}$)	b ($^{\circ}$)	m-M (mag)	ρ_1 ($M_{\odot} \text{ kpc}^{-3}$)	σ_{ρ_1} ($M_{\odot} \text{ kpc}^{-3}$)	ρ_2 ($M_{\odot} \text{ kpc}^{-3}$)	σ_{ρ_2} ($M_{\odot} \text{ kpc}^{-3}$)	ρ_3 ($M_{\odot} \text{ kpc}^{-3}$)	σ_{ρ_3} ($M_{\odot} \text{ kpc}^{-3}$)
110.0	-34.5	11.1	0.0	4.76E5	0.0	5.00E3	1.28E7	5.12E6
110.0	-34.5	11.3	0.0	1.16E5	0.0	6.86E5	3.14E6	3.01E6
110.0	-34.5	11.5	0.0	1.51E5	0.0	2.75E5	5.74E6	1.87E6
110.0	-34.5	11.7	1.11E5	1.34E5	0.0	7.00E4	0.0	1.28E6
110.0	-34.5	11.9	2.36E5	2.00E5	0.0	6.49E4	5.1E5	6.46E5

NOTE. — Densities ρ_1 , ρ_2 and ρ_3 correspond to the mass densities for the template populations with $[\text{Fe}/\text{H}] = -2.2$, -1.3 and -0.7 , respectively. The densities in this table correspond to the Salpeter IMF (Salpeter 1955) used by the MATCH software and are in solar masses per cubic kiloparsec, unlike the densities quoted in the text of the paper, which are corrected for a Kroupa IMF (Kroupa et al. 1993) and in solar masses per cubic parsec. The remainder of this table are available online.

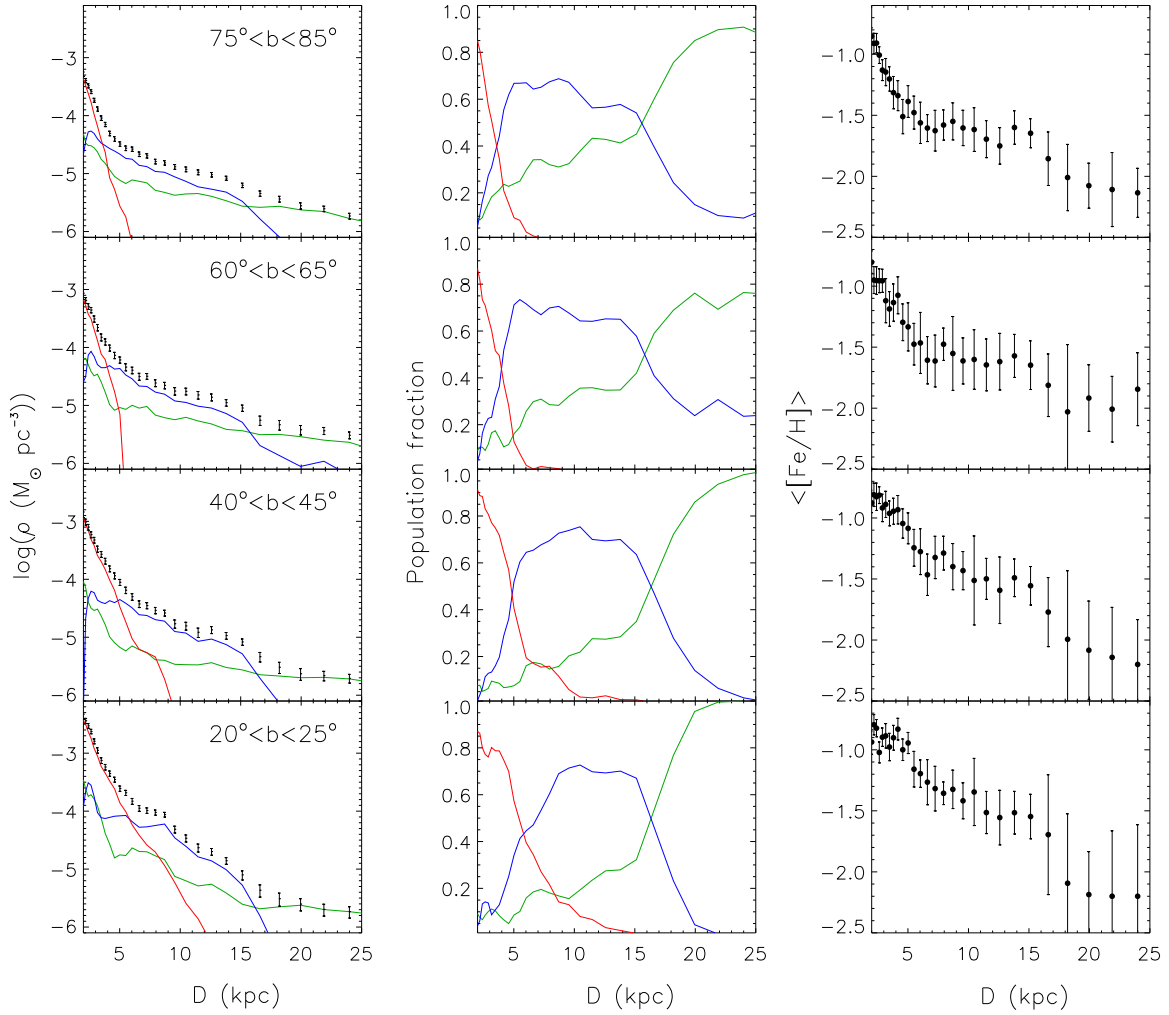


FIG. 7.— Mean stellar mass densities and metallicities as function of distance. The left-hand panels show the total stellar mass density with the black error bars for four different bins in Galactic latitude, indicated in the top right of each panel, and averaged over all longitudes. Colored lines show the mass density in the individual template populations with red for the ‘thick-disk-like’, blue for the ‘inner-halo-like’ and green for the ‘outer-halo-like’ population. In the middle panels the colored lines follow the same color scheme to indicate the fractional contribution of the individual template populations to the total mass density, for the same latitude bins. The right-hand panels show the mass-weighted mean metallicity, again for the same latitude bins as in the left-hand panels.

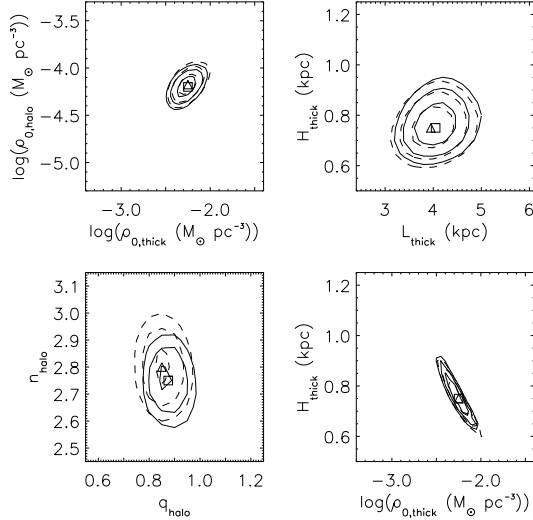


FIG. 8.— Results of fitting smooth Galactic models to the stellar density maps. For the case where all data are used, the best fit values are indicated with squares and iso- χ^2 contours are plotted with solid lines. Triangles and dashed contours are for the case when the Sagittarius stream and the Monoceros overdensity are excised. In both cases, contours are scaled to correspond to the 1, 2 and 3σ uncertainties determined through bootstrap tests.

Near the position of the original discovery, this structure can also be seen in Figure 5: particularly in the $l=178^\circ$ and $l=187^\circ$ stripes a ‘bump’ is apparent in the stellar density at $5 < D < 10$ kpc and $0 < Z < 5$ kpc.

To test for the influence of these structures on the fit results, we fit the density maps twice, once with all data, and once without the regions dominated by these structures. The regions that are excised to remove the impact of the Sagittarius stream and Monoceros are listed in Table 2, amounting to $\sim 4\%$ of all data points.

The role of the thin disk is limited by only looking at the area at $|Z| > 1.0$ kpc, and we fix its parameters at $L_{thin}=2.6$ kpc and $H_{thin}=0.25$ kpc, following Jurić et al. (2008) and in line with earlier star count results (e.g. Siegel et al. 2002). In other words, we treat the thin disk as a known and fixed ‘perturbation’ to our CMD analysis. Using $R_\odot=7.6$ kpc (Vallée 2008)⁷, we are now left with seven free parameters in fitting the total stellar mass density (summed over the three metallicity components): the thick disk parameters f_{thick} , L_{thick} and H_{thick} , the halo parameters f_{halo} , q_{halo} and n_{halo} and the local thin disk density $\rho_{thin,\odot}$. The latter serves as normalization for the thick disk and halo density, hence in practice reducing the number of free parameters to six.

In Table 3 we list the parameter values corresponding to the best fits, with the mass densities scaled to a Kroupa-like IMF (Kroupa et al. 1993). The best fit to all data has a reduced χ^2 of 4.2, and the best fit to the data without Sagittarius and Monoceros has a reduced χ^2 of 3.9. Inclusion of these structures thus has a noticeable impact on the goodness-of-fit, but in both cases the smooth models provide a poor description of the data, in line with Bell et al. (2008) and Jurić et al. (2008). Since

⁷ As R_\odot is still not very well determined (e.g. Bovy et al. 2009), we have also used values of 7.1 and 8.1 kpc for R_\odot and found the effects of these changes on the fit results to be negligible compared to the uncertainties quoted in Table 3.

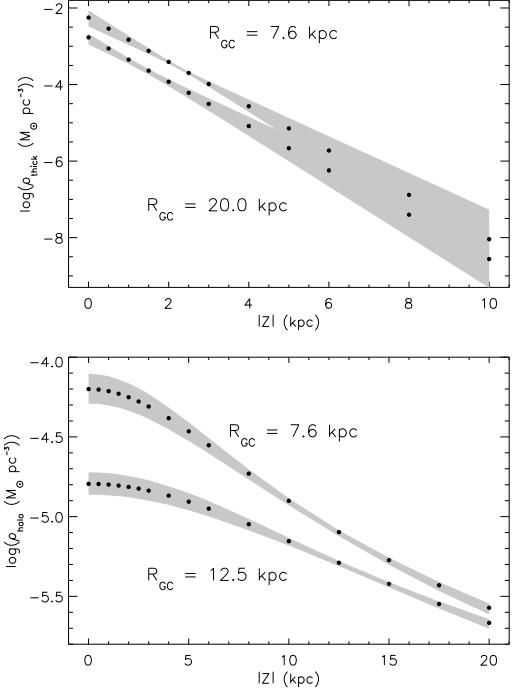


FIG. 9.— Thick disk (top) and halo (bottom) densities in the best-fit smooth model as function of distance from the Galactic plane. The densities were calculated for two galactocentric radii, 7.6 kpc (the assumed galactocentric radius of the Sun) and 12.5 kpc, and the sequences of points are labeled accordingly. Dots show the density at each location for the best-fit model, while the grey areas show the 95% confidence region determined from the bootstrap analysis.

this inhibits deriving proper confidence intervals based on the χ^2 statistic, the uncertainties on the fit parameters listed in Table 3 were obtained by bootstrap resampling tests, in which the ‘pixels’ in the density maps were resampled. In Figure 8 we present the contour plots of the 1σ , 2σ and 3σ (68%, 95% and 99.7%) confidence levels around the fit parameters, which are also based on the bootstrap analysis.

The local mass densities of the thick disk ($\rho_{thick,\odot} = 10^{-2.3 \pm 0.1} M_\odot \text{pc}^{-3}$) and halo ($\rho_{halo,\odot} = 10^{-4.20 \pm 0.05} M_\odot \text{pc}^{-3}$) are not directly constrained by the data, but are extrapolations from data at higher $|Z|$ and R_{GC} . The mass densities of thick disk and halo are much better constrained at longer distances, as demonstrated in Figure 9, where the best model densities and their 95% confidence intervals are plotted at different locations. The thick disk density is best constrained at $(R_{GC}, |Z|) = (7.6, 2.5)$ kpc as $\rho_{thick} = 10^{-3.70 \pm 0.02} M_\odot \text{pc}^{-3}$, and the halo density at $(R_{GC}, |Z|) = (10.0, 12.5)$ kpc as $\rho_{halo} = 10^{-5.19 \pm 0.01} M_\odot \text{pc}^{-3}$ ($10^{-5.21 \pm 0.01} M_\odot \text{pc}^{-3}$ when Sagittarius and Monoceros are omitted). These formal errors are presumably exceeded by uncertainties in the IMF and by substructure.

Recent dynamical modeling (e.g. Flynn et al. 2006) implies a local thick disk density of $10^{-2.46} M_\odot \text{pc}^{-3}$ and a local halo density of $10^{-4} M_\odot \text{pc}^{-3}$, similar to our findings. However, our local mass densities include stellar remnants, and a proper comparison should take this into account. The total local mass density, dominated by the thin disk, in stars and white dwarfs is $\sim 0.038 M_\odot \text{pc}^{-3}$ (Flynn et al. 2006), and star count studies typically give

thick disk and halo normalizations w.r.t. the thin disk of 1 to 10% and 0.1 to 0.2%, respectively (Siegel et al. 2002). This therefore implies a local density, including remnants, of $10^{-3.40}$ to $10^{-2.42} M_{\odot}\text{pc}^{-3}$ for the thick disk and $10^{-4.42}$ to $10^{-4.12} M_{\odot}\text{pc}^{-3}$ for the stellar halo, values that are consistent with our density estimates. If we normalize our findings by the local value from Flynn et al. (2006), we find local thick disk and halo mass density fractions of $15\pm4\%$ and $0.17\pm0.03\%$, respectively. Jurić et al. (2008), in their analysis of SDSS data, find $12\pm1\%$ for the thick disk, consistent with our results, and $0.51\pm0.13\%$ for the halo, inconsistent at the 2.6σ level. These normalizations also imply that the stellar density of the thin disk should never amount to more than $\sim 10\%$ at $|Z| > 1.5$ kpc in our maps, confirming that it is merely a perturbation to our analysis at these locations.

Thick disk structural parameters determined previously through star count studies have shown a large spread (e.g. Siegel et al. 2002). Scale heights vary from ~ 0.6 to ~ 2.0 kpc, but with the more recent measurements converging to the lower end of this range, and scale lengths vary from 2.8 to 4.3 kpc. Jurić et al. (2008) find very different values depending on the tracer stars or photometric parallax relations that are used, but settle on 0.9 ± 0.2 kpc and 3.6 ± 0.7 kpc for the thick disk scale height and length. Through our present analysis, we have been able to estimate the scale length and height of the thick disk to 10% accuracy: $L_{\text{thick}} = 4.1\pm0.4$ kpc and $H_{\text{thick}} = 0.75\pm0.07$ kpc. This is consistent with but more precise than previous determinations, and in good agreement with the work of Jurić et al. (2008).

Halo parameters, when described by a single power-law, are probably varying with radius (e.g. Bell et al. 2008; Watkins et al. 2009; Sesar et al. 2009), and in this study only the stellar halo within a radius of 25 kpc from the Sun has been considered. Two recent studies based on SDSS data have measured the flattening and power-law index of the stellar halo. Jurić et al. (2008), reaching to $\simeq 20$ kpc, find a halo flattening parameter of $q_h=0.64$ and a power-law index of $n_h=2.77$ with quoted uncertainties of $\lesssim 0.1$ and $\lesssim 0.2$, respectively. Bell et al. (2008) find that a q_h of 0.6 to 0.7 gives the least excess rms scatter around their model fits, but that a q_h of 0.7 to 0.8 gives the best χ^2 values. In either case, the constraints on q_h are weak. The halo model used by Bell et al. (2008) has a broken power-law, with independent indices on either side of the break radius. These parameters are also weakly constrained, with the preferred break radius lying between 20 and 30 kpc, the inner power-law index between 2 and 3, and the outer power-law index between 3 and 4. Similarly, Watkins et al. (2009) use RR Lyrae variable stars in SDSS Stripe 82 to infer $n_h=-2.4$ within 23 kpc and $n_h=-4.5$ at larger distances. By comparison, our analysis yields very precise measurements of $n_h = 2.75 \pm 0.07$ and $q_h = 0.88 \pm 0.03$ for the stellar halo within 25 kpc from the Sun. While our value for the power-law index is in excellent agreement with Jurić et al. (2008) and the inner power-law index from Bell et al. (2008), we find the stellar halo to be less flattened. Note that these previous SDSS determinations were restricted to $b \gtrsim 30^\circ$; the inclusion of the SEGUE scans across the Galactic plane boosts the power to de-

TABLE 2
REGIONS EXCISED FOR 2ND MODEL FIT

Structure	l ($^\circ$)	b ($^\circ$)	$m - M$ (mag)
Sgr stream	94	< -65	> 16.0
Sgr stream	178	$-65 - 25$	> 16.5
Sgr stream	229	$+55 - 70$	> 15.5
Sgr stream	270	$+55 - 70$	> 15.5
Sgr stream	300	$+58 - 72$	> 15.5
Sgr stream	330	$+60 - 80$	> 15.5
Monoceros	178	$+15 - 35$	$14.0 - 16.0$
Monoceros	187	$+15 - 35$	$14.0 - 16.0$

TABLE 3
SMOOTH GALACTIC MODEL FITS

Parameter	Full data	Exclude Sgr, Mon
$\rho_{\text{thick}, \odot} (M_{\odot}\text{pc}^{-3})$	$10^{-2.3\pm0.1}$	$10^{-2.3\pm0.1}$
L_{thick} (kpc)	4.1 ± 0.4	4.0 ± 0.4
H_{thick} (kpc)	0.75 ± 0.07	0.75 ± 0.08
$\rho_{\text{halo}, \odot} (M_{\odot}\text{pc}^{-3})$	$10^{-4.20\pm0.05}$	$10^{-4.18\pm0.05}$
q_{halo}	0.88 ± 0.03	0.85 ± 0.03
n_{halo}	2.75 ± 0.07	2.80 ± 0.08

termine flattening.

4.2. Substructure, or deviations from a smooth model

To focus on substructure in the stellar halo and thick disk we now subtract the best-fit smooth model to the complete data set from the density maps in Figure 5. The residuals after subtracting this smooth model are shown in Figure 10, revealing a wealth of substructure. In principle the CMD fitting method can provide not only the stellar densities, but also yield information on the stellar populations of overdensities, for example their metallicities. However, the reconstruction of such stellar population properties after model differencing requires a more detailed study of specific structures than the current analysis, which is based on three simple template populations. Therefore we limit ourselves here to a short description of the main structures responsible for the overdensities seen in Figure 10.

Sagittarius stream. Probably the most striking stellar ‘substructure’ in the Galactic halo, the Sagittarius stream (labeled with an ‘S’ in Fig. 10) is visible in several stripes, both in the northern and the southern Galactic hemisphere. The northern arm is clearly visible in the stripes at $l=229^\circ$, 270° , and 300° , at and just outside the dashed semicircles marking a distance of 25 kpc. At $l=330^\circ$ the stream is more distant (cf. Belokurov et al. 2006) and off the plot. The two arms in which this part of the stream is split (Belokurov et al. 2006) are detected very clearly, particularly in the $l=270^\circ$ stripe. Typical peak densities in these stripes are 5 to $8 \times 10^{-6} M_{\odot}\text{pc}^{-3}$. At $l=203^\circ$ the northern Sgr stream should enter the stripe around $b=30^\circ$ and plunge into the disk (cf. Belokurov et al. 2006; Yanny et al. 2009b). As it is roughly equidistant with the Low-Latitude Stream, it is difficult to distinguish it in the overdensity at low latitudes in this stripe. In the southern Galactic cap, the Sgr stream yields strong detections in two stripes, namely the $l=94^\circ$ and 178° stripes, re-

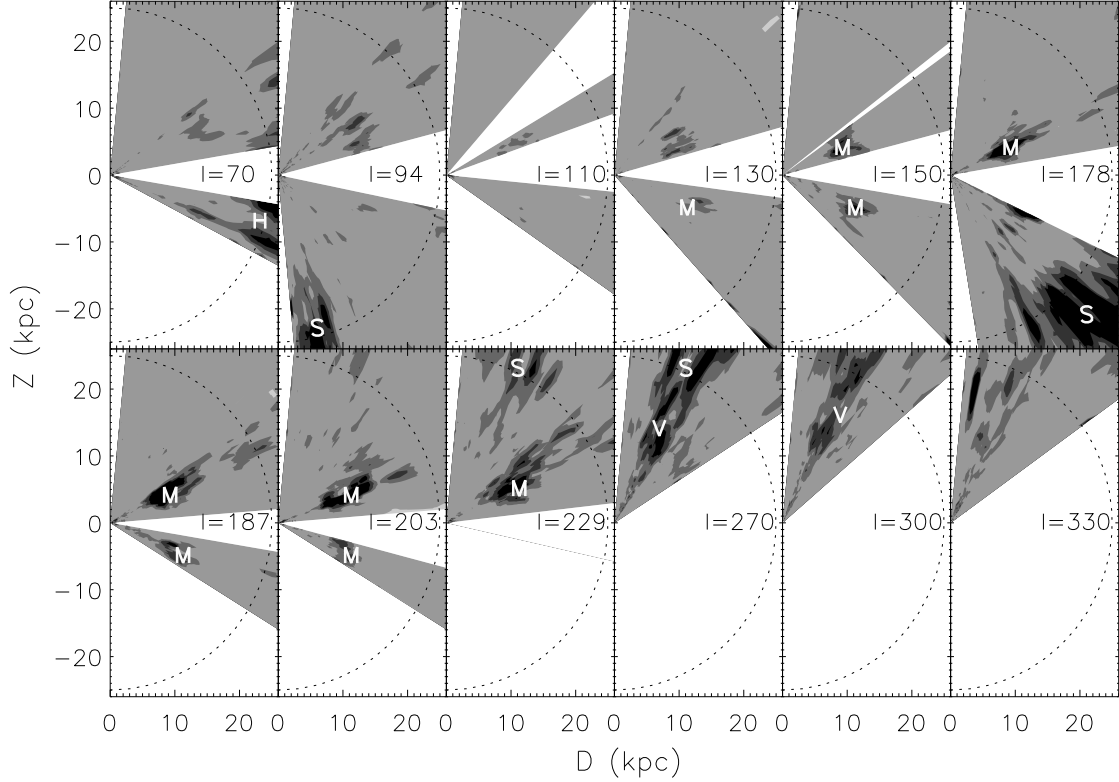


FIG. 10.— Residual stellar mass density after subtraction of a smooth Galactic model. Panel layout is the same as in Figure 5. Starting from black, the grayscale levels correspond to areas with residual densities > 3 , $3-2$, $2-1$, $1-0$, and < -1 times the model density. White areas contain no information due to an absence of data or too high reddening. The dashed semicircles show the distance up to where fit results are (mainly) based on main-sequence turn-off star colors and densities. Four known overdensities are labeled: the Sagittarius stream (S), the Virgo overdensity (V), the Hercules-Aquila cloud (H), and the Monoceros, or Low Latitude stream (M).

producing the detection by Yanny et al. (2009b). Here the stream is also seen at distances of 20 kpc and higher. The density of the stream in these southern detections peaks at $\sim 1 \times 10^{-5} M_{\odot} \text{pc}^{-3}$, slightly higher than in the North Galactic cap.

Virgo. The Virgo overdensity (Jurić et al. 2008) is another strong overdensity in the Northern Galactic cap, centered at $(l, b) \simeq (280^{\circ}, 70^{\circ})$ and extending between distances of ~ 10 to ~ 20 kpc (Bell et al. 2008; Jurić et al. 2008). It is very prominent in the residual maps of the stripes at $l=270^{\circ}$ and 300° in the same direction as the Sgr stream, but at distances less than 20 kpc. The overdensities at similar distances in the $l=330^{\circ}$ stripe might be related to Virgo as well. Typical densities in the Virgo overdensity we find in the $l=270^{\circ}$ and 300° stripes are $\sim 2 \times 10^{-5} M_{\odot} \text{pc}^{-3}$, peaking at around $\sim 4 \times 10^{-5} M_{\odot} \text{pc}^{-3}$.

Hercules-Aquila. A large overdensity extending both above and below the disk and spanning $\sim 80^{\circ}$ in longitude was detected by Belokurov et al. (2007) and christened the Hercules-Aquila cloud. This structure is centered at $l \simeq 40^{\circ}$, but is visible out to $l \lesssim 90^{\circ}$ (Belokurov et al. 2007). The strong overdensities detected at $l=70^{\circ}$ and $b > -25^{\circ}$ or $(D, Z) \simeq (23, -10)$ can therefore be attributed to this recently discovered stellar component.

Monoceros and Low Latitude Stream. The Monoceros structure was first discovered in SDSS data by Newberg et al. (2002) as a strong stellar overdensity at $(l, b) \simeq (200^{\circ}, 20^{\circ})$. Later such overdensities were detected over a large range of Galactic longitudes both

above and below the Galactic plane, always at low latitudes and roughly equidistant, thus forming a ring-like structure around the Milky Way (Ibata et al. 2003; Yanny et al. 2003; Conn et al. 2005, 2007). In the stripes at the longitudes corresponding to the original discovery, $l=178^{\circ}$, 187° , and 203° , the overdensity is detected at high significance at heliocentric distances of roughly 10 kpc and ~ 3 kpc above the Galactic plane. The ring-like nature of the Low Latitude Stream appears to be confirmed by our new map, as overdensities at the same heliocentric distances and latitudes are present in the stripes at $l=130^{\circ}$, 150° and 229° . The density of the structure is highest in the stripes at $l=178^{\circ}$, 187° , and 203° , where the maximum density reached is $\sim 1.5 \times 10^{-4} M_{\odot} \text{pc}^{-3}$. Both in the stripes at lower and higher longitudes the density seems to fall off by a factor of $\simeq 2$. The overdensity detections at negative latitudes (Ibata et al. 2003; Conn et al. 2005, 2007) are confirmed here, with an overdensity detected consistently ~ 4 kpc below the plane from $l=130^{\circ}$ to $l=203^{\circ}$. Below the plane the overdensities have lower densities than above the plane, increasing from $\sim 0.2 \times 10^{-4} M_{\odot} \text{pc}^{-3}$ at $l=130^{\circ}$ to $\sim 1.3 \times 10^{-4} M_{\odot} \text{pc}^{-3}$ at $l=130^{\circ}$.

Unknown substructure. In a few locations less prominent substructures are visible, that cannot directly be identified with known overdensities. Most of these are located at low latitudes and might be related to the Low Latitude Stream. In a future publication we will study these overdensities and their possible connection with the Low Latitude Stream in detail.

5. SUMMARY AND CONCLUSIONS

We have applied CMD-fitting techniques to SEGUE photometric data to study the stellar structure of the Galaxy at both high and low latitudes. Using three template stellar populations, a detailed, three dimensional census of stellar mass is obtained. A change of turn-off color is seen in the halo at distances of 15 to 20 kpc, and can be explained by a change in mean metallicity (Fig. 7). At distances smaller than ~ 10 kpc our results indicate a mean metallicity of $[\text{Fe}/\text{H}] \sim -1.6$, similar to the work by Ivezić et al. (2008), who find a value of $[\text{Fe}/\text{H}] \sim -1.5$ out to ~ 9 kpc. At larger distances, $D \gtrsim 15$ kpc, our results indicate that the mean metallicity of the stellar halo is $[\text{Fe}/\text{H}] \sim -2.2$, however. This change in in-situ population properties is consistent with the inference from nearer ($D \lesssim 4$ kpc) stars by Carollo et al. (2007) and preliminary results from Beers et al. (2009). Structural parameters of the Galaxy can be derived from the resulting stellar density maps through the comparison with models. Our fits of models with an exponential thin and thick disk and a power-law halo (Eq. 2) yield constraints on the thick disk local density, $\rho_{\text{thick},\odot}$, scale height, H_{thick} , and scale length, L_{thick} , and the halo local density, $\rho_{\text{halo},\odot}$, flattening, q_{halo} and power-law index, n_{halo} . As pointed out by Belokurov et al. (2006), Bell et al. (2008) and Jurić et al. (2008), the SDSS data of the stellar halo contains clear evidence of the presence of substructure with respect to smooth halo models. Bell et al. (2008) also demonstrated that the larger known substructures in the halo significantly influence their model fits. To test the sensitivity of our model fits to known substructure, we perform our fits to the full data set, as well as to a data set with the Sagittarius stream and Monoceros overdensity removed. The results are tabulated in Table 3, and are not strongly influenced by the presence of these structures. In either case, the reduced χ^2 of the best fit, 4.2 and 3.9, shows that the smooth model is a poor fit to the data.

The values we find for the local density of the thick disk, $\rho_{\text{thick},\odot} = 10^{-2.3 \pm 0.1} M_{\odot} \text{pc}^{-3}$ and the local halo density, $\rho_{\text{halo},\odot} = 10^{-4.20 \pm 0.05} M_{\odot} \text{pc}^{-3}$, agree well with star count studies. Also our results for the thick disk structural parameters, $H_{\text{thick}} = 0.75 \pm 0.07$ kpc and $L_{\text{thick}} = 4.1 \pm 0.4$, are well within the range of parameters found in previous studies (Siegel et al. 2002) and consistent with the results of Jurić et al. (2008). In the flattening of the stellar halo, where we find $q_{\text{halo}} = 0.88 \pm 0.04$, our analysis seems to divert from the work by Bell et al. (2008) and Jurić et al. (2008), who use SDSS data to study the halo out to similar distances. On the other hand, the power-law index we recover, $n_{\text{halo}} = 2.75 \pm 0.07$, is in excellent agreement.

Subtracting the best model from the stellar density maps unveils abundant substructure (Fig. 10). Most of the overdensities seen can be attributed to known structures in the halo and outer disk of the Galaxy: the Sagittarius stream, Virgo overdensity, and the Monoceros overdensity or Low Latitude Stream. Whereas the origin of the Sagittarius stream is known to be the result of the disruption of the Sagittarius dwarf galaxy, the nature of the other two entities is under debate, and particularly the interpretation of the overdensities at low Galactic latitudes is contentious. A detailed analysis of all substructures is outside the scope of this paper, but an in-depth study of the low latitude substructure is planned to be presented in a future publication.

The authors thank Eric Bell and Constance Rockosi for stimulating and helpful conversations and Sergey Koposov for logistical help. We are also grateful for helpful comments and feedback from Željko Ivezić and Mario Jurić. J.T.A.d.J. was supported by DFG Priority Program 1177. T.C.B. acknowledges partial support for this work from grant PHY 08-22648: Physics Frontier Center/Joint Institute for Nuclear Astrophysics (JINA), awarded by the U.S. National Science Foundation.

Funding for the SDSS and SDSS-II has been provided by the Alfred P. Sloan Foundation, the Participating Institutions, the National Science Foundation, the U.S. Department of Energy, the National Aeronautics and Space Administration, the Japanese Monbukagakusho, the Max Planck Society, and the Higher Education Funding Council for England. The SDSS Web Site is <http://www.sdss.org/>.

The SDSS is managed by the Astrophysical Research Consortium for the Participating Institutions. The Participating Institutions are the American Museum of Natural History, Astrophysical Institute Potsdam, University of Basel, University of Cambridge, Case Western Reserve University, University of Chicago, Drexel University, Fermilab, the Institute for Advanced Study, the Japan Participation Group, Johns Hopkins University, the Joint Institute for Nuclear Astrophysics, the Kavli Institute for Particle Astrophysics and Cosmology, the Korean Scientist Group, the Chinese Academy of Sciences (LAMOST), Los Alamos National Laboratory, the Max-Planck-Institute for Astronomy (MPIA), the Max-Planck-Institute for Astrophysics (MPA), New Mexico State University, Ohio State University, University of Pittsburgh, University of Portsmouth, Princeton University, the United States Naval Observatory, and the University of Washington.

REFERENCES

- Abazajian, K. N., Adelman-McCarthy, J. K., Agüeros, M. A., Allam, S. S., Allende Prieto, C., et al. 2009, *ApJS*, 182, 543
Bahcall, J. N. & Soneira, R. M. 1980, *ApJS*, 44, 73
Beers, T. C., An, D., Johnson, J. A., Pinsonneault, M. H., Terndrup, D. M., Delahaye, F., Lee, Y. S., Masseron, T., et al. 2009, *arXiv:0910.4731*
Bell, E. F., et al. 2008, *ApJ*, 680, 295
Bellazzini, M., Ibata, R. A., Martin, N., Lewis, G. F., Conn, B., Irwin, M. J., 2006, *MNRAS*, 366, 865
Belokurov, V., et al. 2006, *ApJ*, 642, L137
Belokurov, V., et al. 2007, *ApJ*, 657, L89
Bonifacio, P., Monai S. & Beers, T. C., Bovy, J., Hogg, D. W. & Rix, H.-W. 2009, *ApJ*, 704, 1704
Carollo, D., et al. 2007, *Nature*, 450, 1020
Chiba, M. & Beers, T. C. 2000, *AJ*, 119, 2843
Conn, B. C., Lewis, G. F., Irwin, M. J., Ibata, R. A., Ferguson, A. M. N., Tanvir, N. & Irwin, J. M., 2005, *MNRAS*, 362, 475
Conn, B. C., et al. 2007, *MNRAS*, 376, 939
de Jong, J. T. A., Butler, D. J., Rix, H.-W., Dolphin, A. E. & Martínez-Delgado, D., 2007, *ApJ*, 662, 259
de Jong, J. T. A., Rix, H.-W., Martin, N. F., Zucker, D. B., Dolphin, A. E., Bell, E. F., Belokurov, V. & Evans, N. W., 2008, *AJ*, 135, 1361
Dolphin, A. E. 1997, *New A*, 2, 397

- Dolphin, A. E. 2001, MNRAS, 332, 91
- Eggen, O. J., Lynden-Bell, D. & Sandage, A. R. 1962, ApJ, 136, 748
- Flynn, C., Holmberg, J., Portinari, L., Fuchs, B. & Jahreiß, H. 2006, MNRAS, 372, 1149
- Gilmore, G. & Reid, N. 1983, MNRAS, 202, 1025
- Girardi, L., Grebel, E. K., Odenkirchen, M., & Chiosi, C. 2004, A&A, 422, 205
- Grillmair, C. J. 2006, ApJ, 651, L29
- Gunn, J.E. et al. 1998, AJ, 116, 3040
- Gunn, J.E. et al. 2006, AJ, 131, 2332
- Herschel, W. 1785, RSPT, 75, 213
- Hogg, D.W., Finkbeiner, D.P., Schlegel, D.J., & Gunn, J.E. 2001, AJ, 122, 2129
- Ibata, R. A., Irwin, M. J., Lewis, G. F., Ferguson, A. M. N. & Tanvir, N. 2003, MNRAS, 340, L21
- Ivezić, Ž. et al. 2004, AN, 325, 583
- Ivezić, Ž. et al. 2008, ApJ, 684, 287
- Jurić, M., et al. 2008, ApJ, 673, 864
- Kapteyn, J. C. 1922, CMWCI, 230, 1
- Kazantzidis, S., Bullock, J. S., Zentner, A. R., Kravtsov, A. V. & Moustakas, L. A., 2007, ApJ, subm. (arXiv:0708.1949)
- Kent, S. M., Dame, T. M. & Fazio, G. 1991, ApJ, 378, 131
- Kroupa, P., Tout, C. A. & Gilmore, G. 1993, MNRAS, 262, 545
- Lupton, R., Gunn, J., & Szalay, A. 1999, AJ, 118, 1406
- Majewski, S. R., Skrutskie, M. F., Weinberg, M. D. & Ostheimer, J. C. 2003, ApJ, 599, 1082
- Martin, N. F., Ibata, R. A., Bellazzini, M., Irwin, M. J., Lewis, G. F., & Dehnen, W. 2004, MNRAS, 348, 12
- Martin, N. F., de Jong, J. T. A. & Rix, H.-W., 2008, ApJ, 684, 1075
- Momany, Y., Zaggia, S. R., Gilmore, G., Piotto, G., Carraro, G., Bedin, L. R. & de Angeli, F. 2006, A&A, 451, 515
- Newberg, H. J., et al. 2002, ApJ, 569, 245
- Padmanabhan, N., Schlegel, D. J., Finkbeiner, D. P., Barentine, J. C., Blanton, M. R., et al. 2008, ApJ, 674, 1217
- Pier, J.R., Munn, J.A., Hindsley, R.B., Hennessy, G.S., Kent, S.M., Lupton, R.H., & Ivezić, Z. 2003, AJ, 125, 1559
- Reylé, C., Marshall, D. J., Robin, A. C. & Schultheis, M. 2009, A&A, 495, 819
- Salpeter, E. E. 1955, ApJ, 121, 161
- Schlegel, D., Finkbeiner, D. & Davis, M. 1998, ApJ, 500, 525
- Sesar, B., et al. AJ, 134, 2236
- Sesar, B., Ivezić, Z., Grammer, S. H., Morgan, D. P., Becker, A. C., Jurić, M., De Lee, N., Annis, J., et al. 2009, arXiv:0910.4611
- Siegel, M. H., Majewski, S. R., Reid, I. N. & Thompson, I. B., 2002, ApJ, 578, 151
- Smith, J. A., et al. 2002, AJ, 123, 2121
- Stoughton, C. et al. 2002, AJ, 123, 485
- Tucker, D., et al. 2006, AN, 327, 821
- Vallée, J. P., 2008, AJ, 135, 1301
- Watkins, L. L., Evans, N. W., Belokurov, V., Smith, M. C., Hewett, P. C., Bramich, D. M., Gilmore, G. F., Irwin, M. J., et al. 2009, MNRAS, 398, 1757
- Yanny, B., et al. 2003, ApJ, 588, 824
- Yanny, B., Rockosi, C., Newberg, H. J., Knapp, G. R., Adelman-McCarthy, J. K., et al. 2009a, AJ, 137, 4377
- Yanny, B., Newberg, H. J., Johnson, J. A., Lee, Y. S., Beers, T. C., Bizyaev, D., Brewington, H., Re Fiorentin, P., et al. 2009b, ApJ, 700, 1282
- York, et al. 2000, AJ, 120, 1579
- Younger, J. D., Besla, G., Cox, T. J., Hernquist, L., Robertson, B., & Willman, B., 2008, ApJ, 676, L21